Spectroscopic and adsorptive studies of a thermally robust pyrazolato-based PCP

Spectroscopic and adsorptive studies of a thermally robust pyrazolato-based PCP

Lorenzo Mino, Valentina Colombo, Jenny G. Vitillo, Carlo Lamberti, Silvia Bordiga, Erik Gallo, Pieter Glatzel, Angelo Maspero, Simona Galli

Dalton Trans., 2012, **41**, 4012–4019

DOI: **10.1039/c2dt12121b**

Spectroscopic and adsorptive studies of a thermally robust pyrazolato-based PCP

Lorenzo Mino,[a] Valentina Colombo,[b] Jenny G. Vitillo,[a] Carlo Lamberti,[a] Silvia Bordiga,[a]* Erik Gallo,[a,c,d] Pieter Glatzel,[c] Angelo Maspero,[b] Simona Galli[b]

a) Dipartimento di Chimica Inorganica, Fisica e dei Materiali, Università di Torino, Centre of Excellence and INSTM Centre of Reference, via Quarello 11/A, 10135 Torino, Italy
b) Dipartimento di Scienza e Alta Tecnologia, Università dell'Insubria, via Valleggio 11, 22100 Como, Italy
c) European Synchrotron Radiation Facility (ESRF), 6 Rue Jules Horowitz, BP 220 38043 Grenoble Cedex 9 France
d) Sciences Chimiques de Rennes - UMR 6226, Matériaux Inorganiques: Chimie Douce et réactivité, Université de Rennes 1, Campus de Beaulieu, Bât 10B, F-35042 Rennes, France.

Abstract

The pyrazolato-based PCP $[Ni_8(\mu_4\text{-}OH)_4(\mu_4\text{-}OH_2)_2(\mu_4\text{-}PBP)_6]$ (**NiPBP**, H_2PBP = 4,4'-bis(1*H*-pyrazol-4-yl)biphenyl), whose 3-D architecture is built upon octametallic hydroxo clusters reciprocally connected by the organic spacers, is a very promising candidate for gas adsorption applications, owing to its remarkable thermal stability (up to 400 °C in air) and its high void volume (70%). As such, **NiPBP** was selected as a proof-of-concept material to demonstrate how an optimized set of solid state techniques can concur to create a comprehensive and coherent picture, relating (average and local) structural features to adsorptive properties. To this aim, the response of **NiPBP** toward different gases, retrieved by gas adsorption measurements (N_2 at 77 K, in the low pressure region; H_2 at 77 K, in the high pressure region), was explained in terms of local-level details, as emerged by coupling electronic, X-ray (absorption and emission), and variable temperature IR spectroscopy.

1. Introduction

High permanent porosity, exceptional structural and chemical tunability, and a remarkable thermal stability are the key features of porous coordination polymers (PCPs) which motivated a rapid growth of their popularity[1] immediately after their first appearance in 1995.[2] As a matter of fact, the increasing number of publications devoted to PCPs during the past decade witnesses that these hybrid materials are considered definitely promising for a wide variety of applications: reports focusing on 'classical' applications such as gas storage,[3] gas separation and gas purification,[4] for energy, environmental and medical purposes, have been later on paralleled by investigations of their potential usage as sensors,[5] nano-reactors in heterogeneous catalysis,[6] or nano-carriers for drug delivery and imaging.[7]

The judicious selection of PCPs components (organic spacers and metal-based nodes) generates materials with well-defined chemical and physical properties, *i.e.* suitably designed for specific applications. This enormous flexibility in the synthetic design, and the corresponding richness of structural motifs and functional properties, still represents a challenge in PCPs construction and successive characterization. To understand the structural aspects governing or influencing PCPs functionality, with the final aim of their optimization, a thorough investigation of their structural features is mandatory. In particular, when suitable single crystals are not available, state-of-the-art powder diffraction methods allow to unravel otherwise not accessible key structural aspects.[8] In some cases, this information may be fruitfully complemented by fundamental local-level details, typically concerning the inorganic nodes, retrieved through X-ray (absorption and emission) spectroscopy.[9] Notably, although relatively new, X-ray emission spectroscopy (XES) has already shown its relevance

in the fields of chemistry and materials science for the investigation of the ligands environment of 3*d* transition metals.[10]

Juxtaposing, to this piece of information, complementary observations retrieved by means of other solid state techniques, such as UV-Vis and variable-temperature IR spectroscopy (in the presence, or not, of probe molecules),[11] may give a more complete understanding of the influence of the chemico-physical and structural features of a PCP on its functional properties.

On the other hand, only those materials which couple a specific functionality to a remarkable chemical and thermal inertness are expected to be exploited in suitably devised applications. Our long-term experience in the field of coordination polymers[8] has proved that polyazolates, in which *N*-donor heterocyclic rings are bridged by rigid or flexible aromatic cores, lead to the isolation of materials in which key structural features are coupled to remarkable thermal and chemical stabilities. As a matter of fact, as shown by us and by other research groups,[10,12] *N*-donor spacers offer metal-ligand coordinative bonds which are stronger and less prone to hydrolysis that the *O*-donor counterparts.[13] Worthy of note, this search for robust PCPs containing *N*-donor linkers has clearly demonstrated that pyrazolato-based materials are capable to surpass the imidazolato-, triazolato- and tetrazolato-based analogues.[14]

One notable example in this respect, combining promising structural characteristics to a remarkable thermal stability (up to 400 °C in air), is represented by the coordination polymers $[Ni_8(\mu_4\text{-}OH)_4(\mu_4\text{-}OH_2)_2(\mu_4\text{-}PBP)_6]$ (**NiPBP**) and $[Ni_8(\mu_4\text{-}OH)_4(\mu_4\text{-}OH_2)_2(\mu_4\text{-}TET)_6]$ (**NiTET**) (H_2PBP = 4,4'-bis(1*H*-pyrazol-4-yl)biphenyl; H_2TET = 2,6-bis(1*H*-pyrazol-4-yl)pyrrolo[3,4-*f*]isoindole-1,3,5,7(2*H*, 6*H*)-tetrone).[15] The crystal structure of these two isomorphous species is composed by octanuclear $Ni_8(OH)_4(OH_2)_2(L)_6$ (L = PBP or TET) clusters of cubic symmetry, whose edges are bridged by the pyrazolato residues of the L^{2-} ligands and whose faces are capped either by water molecules or by hydroxo groups (Figure 1a). Each octametallic node is linked to twelve symmetry-related ones within a *fcc* packing (Figure 1b) possessing octahedral and tetrahedral voids of about 1.8 nm and 1.0 nm inner size,[16] respectively, which result in a high void volume, above 70% of the unit cell volume.[17]

NiPBP is thus a promising material for practical applications in the field of gas adsorption. As such, in this report we present a deep investigation of its adsorption properties, employing N_2 (at 77 K in the low pressure region) and H_2 (at 77 K in the high pressure region) as probes. Beside addressing the "average" structural features, the adsorptive response of the material has been interpreted in terms of the local details on the inorganic nodes retrieved by combining electronic spectroscopy to X-ray (absorption and emission) spectroscopy, and in terms of the nature of the adsorption sites, as emerged from variable temperature IR spectroscopy, employing CO and H_2 as probes.

NiPBP thus becomes a valuable *proof-of-concept* material, demonstrating that a complete and coherent picture, relating (average and local) structural aspects to adsorptive properties, can be successfully retrieved through an optimized combination of complementary solid state techniques.

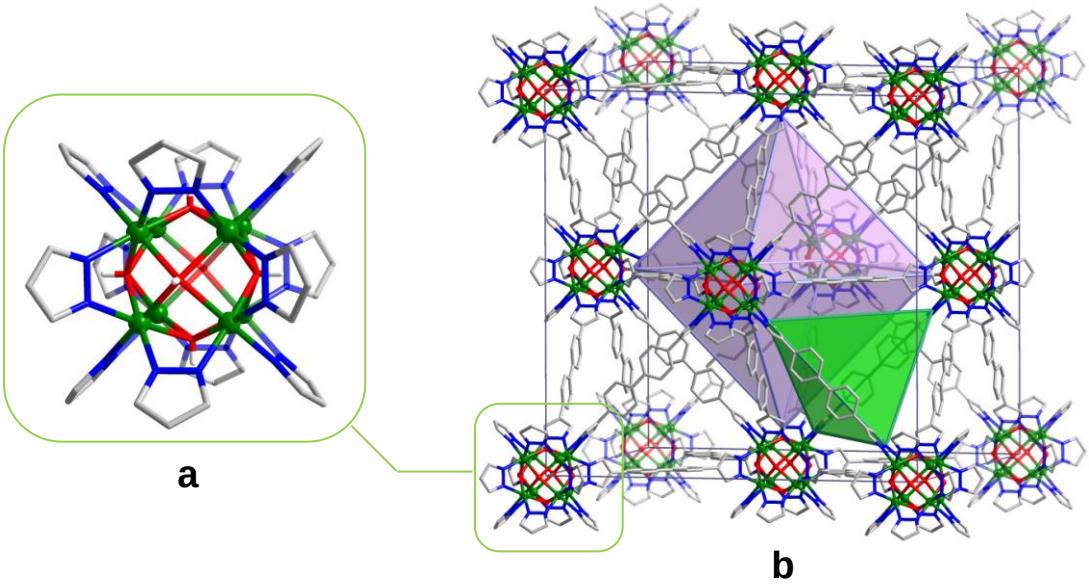

Figure 1. Representation of the crystal structure of **NiPBP**: a) the $Ni_8(OH)_4(OH_2)$ inorganic node; b) a portion of the overall 3-D packing, in which one of the octahedral and tetrahedral cavities have been highlighted. C, grey; H, light grey; Ni, green; N, blue; O, red. The fractional coordinates of the asymmetric unit have been taken from ref. 15. For the sake of clarity, the PBP has depicted according to an ideal ordered model.

2. Results and Discussion

2.1. Gas Adsorption Properties. The gas adsorption performances of **NiPBP** were preliminary verified by collecting N_2 adsorption isotherms at 77 K (Figure 2). The optimally desolvated material was found to absorb significant amounts of N_2 at 77 K, displaying a Type I adsorption isotherm characteristic of materials possessing a microporous nature.

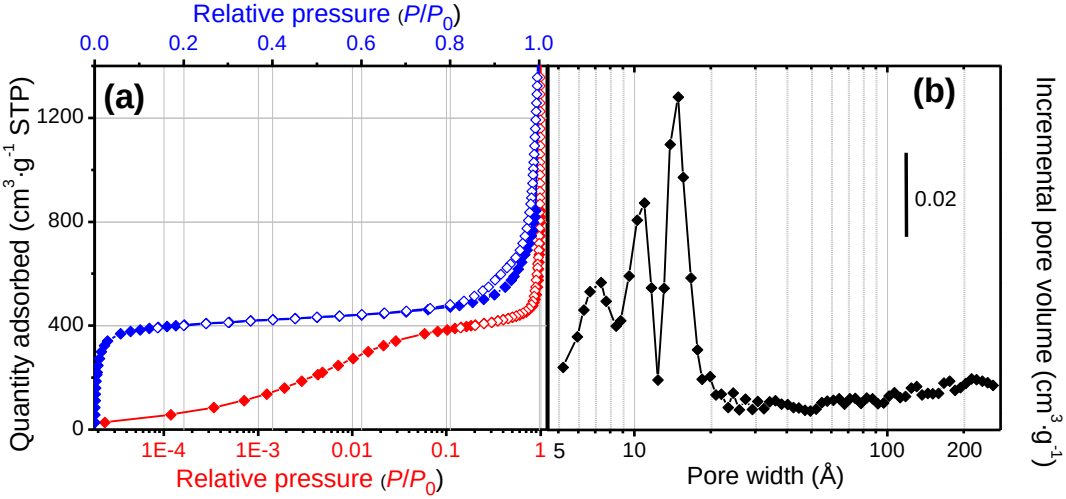

Figure 2. Part (a): Volumetric N_2 adsorption isotherms acquired at 77 K on **NiPBP**. Filled and empty rhombi refer to the adsorption and desorption branches, respectively. Top and bottom abscissa report the same data in linear (blue) and logarithmic (red) scales, respectively, to allow to better appreciate high and low relative pressure ranges. Part (b); Pore distribution obtained by applying the NLDFT method (Non-Local Density Functional Theory, cylindrical pore model, Tarazona) to the N_2 adsorption data in part (a). Note the logarithmic scale of the horizontal axis.

Fitting the N_2 isotherm afforded a BET specific surface area of 1373 m^2/g and a Langmuir specific surface area of 1824 m^2/g, and an impressively high pore volume of 0.80 cm^3/g (Table 1). The contribution of the micropores only can be estimated as 0.56 cm^3/g which is in good agreement with the value of 0.63 cm^3/g retrieved by the crystal structure, thus highlighting that, after proper activation, most of the internal void volume is accessible to the gas probe.

The microporous nature of the sample is confirmed also by both the t-plot and the DFT analysis. In particular, the pore size distribution, as obtained by the DFT approach (Figure 2b), highlights the presence of three distinct ranges of micropore sizes, peaking at 1.5, 1.1 and 0.7 nm. Notably, these dimensions roughly correspond to the diameters of the tetrahedral and octahedral cages of the material, and of their entrance windows, respectively (1.8, 1.0 and 0.5 nm, respectively).

Table 1. Specific surface area S (m^2 g^{-1}) and pore volume V (cm^3 g^{-1}) of **NiPBP**, as retrieved from the N_2 adsorption isotherm at 77 K.

S_{BET} [a]	$S_{Langmuir}$ [b]	S_{micro} [c]	V_{micro} [c]	V_{tot} [d]
1373	1824	1661	0.56	0.80/1.07

[a] Specific surface area evaluated following the BET model in the standard $0.05 < P/P_0 < 0.25$ pressure range.[18] [b] Specific surface area evaluated following the Langmuir model in the standard $0.05 < P/P_0 < 0.25$ pressure range.[18] [c] Micropore area and micropore volume estimated using the t-plot method[18] (adopting the Harkins and Jura thickness curve and taking $S_{Langmuir}$ as reference). [d] Total pore volume calculated as the volume of the hosted probe in the liquid phase (at $p/p_0 \approx 0.90/0.98$).

The high pressure H_2 adsorption isotherm, recorded at 77 K, is shown in Figure 3. The coincidence of the adsorption and desorption branches indicates the full reversibility of the process, which is characterized by a fast kinetics, the equilibrium being reached in less than 5 minutes for each pressure point. This evidence perfectly matches the results emerged from the IR measurements (see below), which exclude the presence of exposed metal sites as possible preferential centers for interactions between the H_2 molecules and the framework.

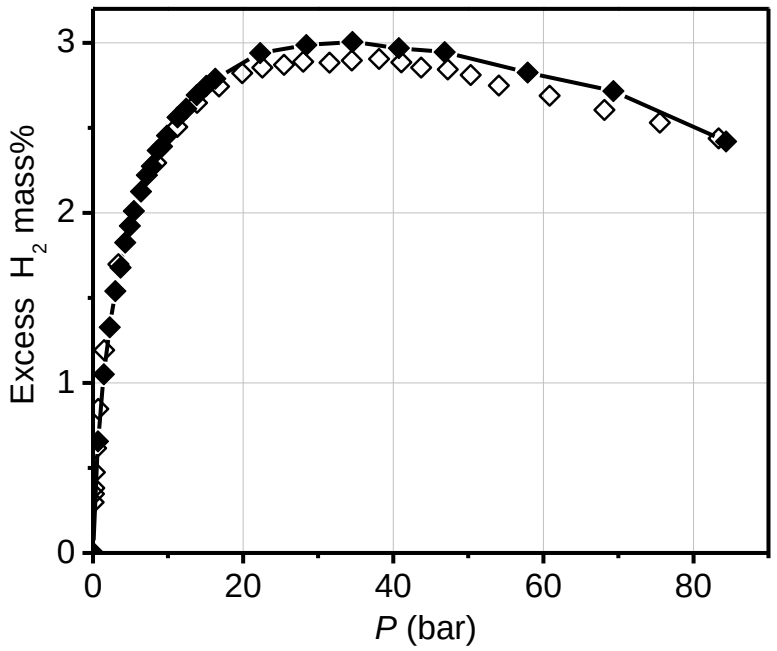

Figure 3. H_2 excess isotherm acquired at 77 K on **NiPBP**. Filled and empty rhombi refer to the adsorption and desorption branches, respectively.

According to the high pressure H_2 adsorption isotherm, at 77 K **NiPBP** exhibits a maximum excess adsorption of 3.0 wt% at 34.5 bar. This uptake, although noteworthy, is sensitively lower than those reported for MIL-101, IRMOF-20 and MOF-177 in the same pressure and temperature conditions (6.1, 6.2 and 7.0 wt%, respectively).[19] The absolute adsorption, calculated using the experimental pore volume of 0.8 cm^3/g retrieved from the porosimetry measurements, reaches values of 3.9 and 4.4 wt% at 34.5 and 84.5 bar, respectively. Alternatively, the absolute adsorption amounts to 3.8 wt% at 84.5 bar if only the microporous volume (0.56 cm^3/g) is considered. Notably, an uptake of 4.4 wt% well agrees with the value theoretically expected assuming the formation of a complete monolayer of H_2 having a close packed *fcc* structure in the close packing limit (4.5 wt%), indicating that, at 77 K and 84.5 bar, the monolayer is completely filled.

2.2. Infrared Spectroscopy. The IR spectrum of the as-synthesized material is dominated by the bands due to the organic spacer - the major absorptions being present in the 3160-2850 and 1790-500 cm^{-1} ranges. In the framework mode region (1790-500 cm^{-1}), more in detail we can recognize: i) a band centered at 815 cm^{-1} due to out-of-plane –CH bending modes; ii) a band centered at 950 cm^{-1} ascribable to in-plane deformations of the phenyl ring; iii) a complex absorption centered at 1100 cm^{-1} associated to in-plane bending of the CH group that belongs to pyrazolate; iv) in the range 1100-1600 cm^{-1} bands due to symmetric and asymmetric stretching modes of the N-N, C-N and C-C bonds are expected; finally, centered at 1650 cm^{-1}, the contribution due the δ mode of H_2O is clearly visible.
As already observed in the case of the **NiTET** homologous,[15] the progressive elimination of water (Figure 4) brings about a sharpening of the absorption band at 3590 cm^{-1}, attributed to the bridging OH groups capping the faces of the Ni_8 polyhedra. Incidentally, this band lies at a significantly lower frequency than that observed for the hydroxyl groups in Ni-based phosphonates,[20] reasonably because of the unusual μ_4-bridging mode adopted by the hydroxyl moieties in **NiPBP** (*vs.* the corresponding μ_4 mode observed in the phosphonates). Notably, the band centered at 3390 cm^{-1}, persisting even after prolonged outgassing at 453 K, must be attributed to the structural water molecules capping the Ni_8 octanuclear clusters, whose removal would provoke the collapse of the framework. According to the crystal structure, the persistence of the water capping molecules in the activated material is not compatible with the formation of exposed metal sites, as already anticipated by the results of H_2 adsorption. Sample activation does not cause any relevant change in the IR spectrum in the framework stretching region, apart from the decrease in intensity of the component ascribable to the bending mode of H_2O (1650 cm^{-1}).

To further strengthen this claim, the reactivity of an activated sample of **NiPBP** was investigated toward carbon monoxide, down to 60 K, and hydrogen, down to 14 K. As evident in Figure 5a, upon CO adsorption, the band at 3590 cm^{-1}, ascribed to the stretching of the hydroxyl groups, is progressively eroded. Concomitantly, a broader component emerges and grows at a lower frequency ($\Delta\nu$ = -57 cm^{-1}), due to the formation of weak hydrogen bond interactions between the OH residues and the probe. At the same time, in the CO stretching frequency region, three distinct components can be appreciated: i) a very weak band growing at 2158 cm^{-1} and easily saturating, suggesting to be associated to defective sites; ii) a more relevant band developing at 2147 cm^{-1}, further confirming the formation of adducts between the hydroxyl groups and the CO molecules; iii) a band at 2134 cm^{-1}, associated to liquid-like CO liquefied inside the PCP cavities. The latter band becomes the major contribution upon progressive increase of the CO equilibrium pressure and, as expected, it is accompanied by the appearance of a band at 2094 cm^{-1}, due to the natural fraction of ^{13}C present in the CO gas. Finally, the absence of any components at higher frequencies excludes the presence of exposed Ni(II) ions, which should easily form Ni(II)···CO adducts, giving a strong band at 2178 cm^{-1}.[27a]

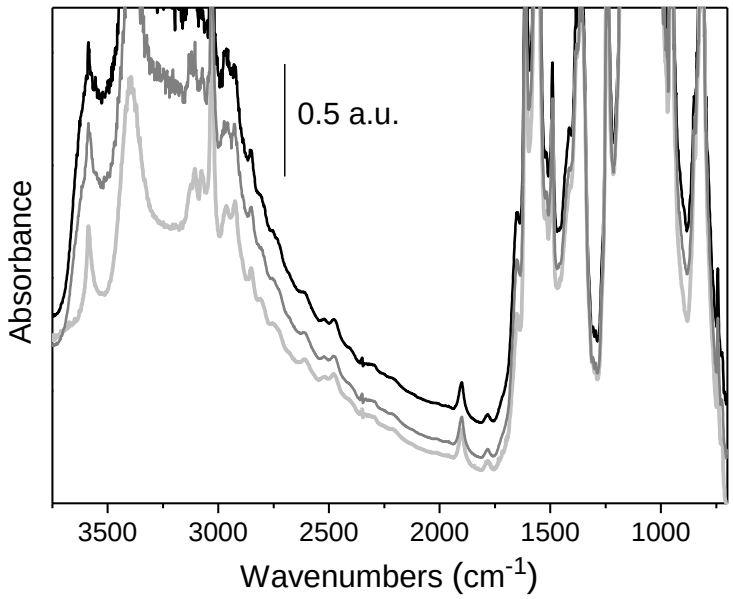

Figure 4. From black to light grey: effect of water removal on the FTIR spectrum of **NiPBP**.

Hydrogen adsorption was monitored on an activated sample of **NiPBP** cooled down to 14 K (Figure 5b). At this point, it is worth recall that the H-H stretching of the H_2 molecule is IR inactive; nevertheless, upon adsorption, the interaction of H_2 with polarisable centres of the host disrupts its symmetry and activates its IR stretching mode, whose red-shift and intensity depend on the strength of the interaction.[21] Upon H_2 dosing, in the region of the OH stretching, the band at 3590 cm^{-1} is partially eroded in favour of the formation of a contribution at a lower frequency ($\Delta\nu$ = -9 cm^{-1}), due to extremely weak hydrogen bond interactions between the residual OH groups and the probe molecule. Concomitantly, we observe the appearance of a band showing an initial shift of -53 cm^{-1} with respect to the Raman H-H stretching frequency of gaseous H_2 (4161 cm^{-1}). Upon increasing coverage, this band progressively moves toward higher frequencies, till reaching a shift of just -25 cm^{-1}. The small value (-53 cm^{-1}) of the maximum observed shift at low coverage is in agreement with the results obtained using CO, confirming the absence of exposed Ni(II) ions. This is further corroborated by the low intensity of the H-H stretching band, which implies a weak interaction of H_2 with the material. Finally, the broad shape of the band, which does not show well defined features, is typical of H_2 weakly interacting with the walls of relatively large micropores, whereas materials with smaller pores exhibit more structured spectra.[29]

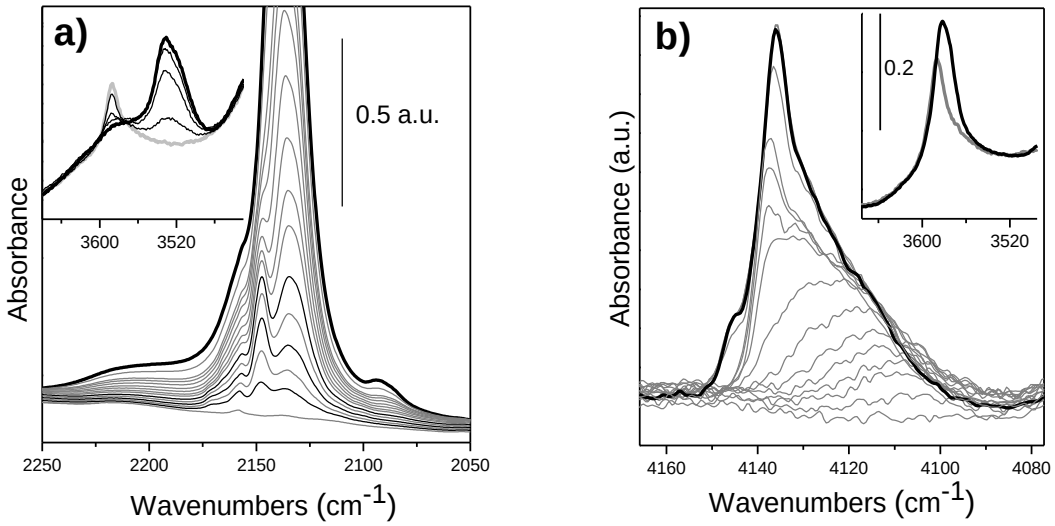

Figure 5. FTIR spectra of (a) CO dosed at 60 K on an activated sample of **NiPBP** and its successive degassing. In the inset, the effect of CO dosing on the OH groups of the PCP is highlighted (the curves acquired at the same coverage in the CO stretching region are reported in black). (b) H_2 dosed at 14 K on an activated sample of **NiPBP** and successive degassing. In the inset, the effect of H_2 dosing on the OH groups of the PCP is highlighted. In both cases, black bold curves represent the maximum coverage.

2.3. Electronic structure: UV-Vis, X-ray Absorption and Emission Spectroscopy. Electronic excitation energies and line shapes provide information on both occupied and unoccupied electronic levels. In particular, the *d-d* transitions (or crystal field excitations), in which only the occupation of the transition metal 3*d* orbitals changes, are sensitive to the local coordination at the metal, thus providing information on the electronic levels involved by the coordination. *d-d* transitions can be investigated by means of optical techniques,[22] electron energy loss[23] and, as in the present study, X-ray absorption near edge structure (XANES)[24] and resonant inelastic X-ray scattering (RIXS).[25] Notably, in spite of the higher preference for *soft* X-ray RIXS, the use of *hard* X-rays has the advantage that high vacuum conditions are not required.

The electronic properties of **NiPBP** were preliminary investigated by means of diffuse reflectance UV-Vis spectroscopy (DRS-UV-Vis). The DRS-UV-Vis spectrum of as-synthesized **NiPBP** (Figure 6b) shows a strong band due to the $\pi\rightarrow\pi^*$ electronic transitions of the organic linker around 28000 cm^{-1}, (3.5 eV) and two weaker components in the region of the CF *d-d* transitions at 9700 cm^{-1} (1.2 eV) and 16000 cm^{-1} (2.0 eV). Possibly, a third one, expected at higher energy in the presence of distorted octahedral Ni(II) ions,[26] can be foreseen around 25000 cm^{-1} (3.1 eV); however, its presence and its exact location cannot be straightforwardly determined from UV-Vis as it is significantly overshadowed by the lower-energy component of the $\pi\rightarrow\pi^*$ transition of the ligand. Upon activation the spectrum changes, testifying a distortion of Ni(II) coordination sphere. In particular in the region of *d-d* transitions the absorption at 9700 cm^{-1} (1.20 eV) splits into two components at 10000 (1.24) and at 6700 cm^{-1} (0.83 eV), while the band at 16000 (2.0 eV) slightly shifts at higher energy. Finally the absorption appearing as a shoulder of the strong band due to the $\pi\rightarrow\pi^*$ electronic transition of the organic linker, ascribed to a further *d-d* transition, becomes more intense, testifying a further distortion of the site upon solvent removal.

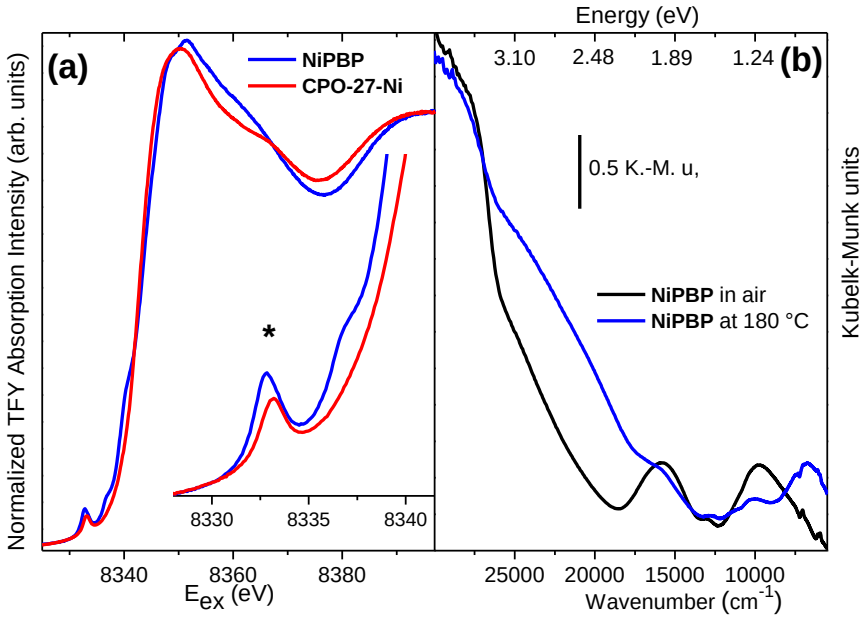

Figure 6. Part (a): Ni K-edge TFY XANES spectra of **NiPBP** and CPO-27-Ni (blue and red curves, respectively). Both curves have been normalized to the edge jump. Part (b): DRS-UV-Vis spectrum of **NiPBP** before (black curve) and after activation at 180 °C (blue curve).

The Ni K-edge XANES spectrum, collected in total fluorescence yield (TFY) of **NiPBP** sample (black curve in Figure 6a) is very similar to that observed for the CPO-27-Ni MOF (red curve), exhibiting a comparable distorted octahedral local environment.[27] In particular, moving from low to high photon energies, at least four groups of transitions are clearly appreciable: i) a weak $1s \rightarrow 3d$ electronic transition at 8332.8 eV (see inset); ii) a second component at 8337.2 eV (see inset); iii) a strong $1s \rightarrow 4p$ dipole-allowed electronic transition near 8340 eV (scarcely visible because too close to the edge jump); vi) a whiteline at 8348 eV (first resonance after the edge). Note that the intensity of the whiteline results slightly depressed when the TFY spectra reported here are compared with those collected in transmission mode,[15,27] due to the self-adsorption effect.

The Ni K-edge RIXS spectrum of **NiPBP** was collected tuning the excitation energy to the energy maximum of the pre-edge peak at 8332.8 eV (star in the inset of Figure 6a), that corresponds to the transition between the ground state electronic configuration of Ni(II), $|\mathbf{g}\rangle 1s^2 3d^8$, to orbitals that have mainly Ni 3*d* character (we therefore write the intermediate state as $|\mathbf{i}\rangle 1s^1 3d^9$). As evident from Figure 7 (see also the scheme in the inset), moving from lower to higher energies, three main features can be identified in the RIXS spectrum: i) the charge transfer region, extending from 8322 eV up to about 8327 eV. If considered as the energy where the spectral intensity has reached half of the first maximum of the charge-transfer band, the charge-transfer energy can be estimated as 8325.7 eV (6.3 eV in energy transfer), in good agreement with published results for Ni(II) in other systems exhibiting O_h-like symmetry.[28] ii) The *d-d* region, where three peaks are clearly visible at 1.25 eV, 1.95 eV and 3.1 eV in energy transfer (see magnification in the inset of Figure 7). iii) The elastic peak, due to the elastic de-excitation transition $|\mathbf{i}\rangle 1s^1 3d^9 \rightarrow |\mathbf{g}\rangle 1s^2 3d^8$.

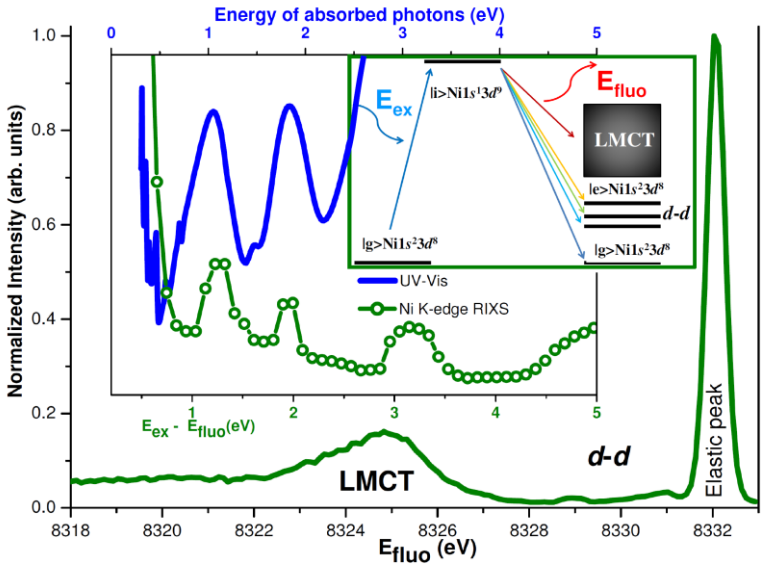

Figure 7. Main part: Ni K-edge RIXS spectrum collected on **NiPBP** with the excitation energy tuned to the energy maximum of the pre-edge peak visible in the inset of Figure 6a (star). To appreciate the weakness of such transitions, also the intensity of the elastic peak at 8332 eV has been reported. Note that this latter is technically not a fluorescence emission. The inset reports the comparison between the Ni K-edge RIXS (green curve, magnified and reported as a function of the energy transfer E_{fluo} - E_{ex}) to allow a direct comparison with the UV-Vis (blue curve) spectrum of **NiPBP**. The cartoon reports a simplified scheme of the two photon process describing the RIXS phenomenon, |**g**>, |**i**> and |**e**> representing the ground, the intermediate and the excited state of the valence *d-d* and/or LMCT transitions. The ground state is formally |**g**> Ni1$s^2$3d^8: the absorption of a photon at 8332 eV promotes an 1*s* electron into an empty 3*d* state. From the intermediate |**i**> Ni1$s^1$3d^9 state, the system evolves either in the ground state again (resulting in the elastic peak), or in an excited |**e**> Ni1$s^2$3d^8 state. The excitation can results in (i) the promotion of a Ni 3*d* electron into an excited 3*d* state, so that the net transition between initial and final states is the same as that obtained in an UV-Vis experiment for a *d- d* excitation; or in (ii) the promotion of an electron from the ligands to the Ni, equivalent to a net LMCT transition.

According to previously performed atomic multiplet calculations,[26] we can confidently assign the peaks at 1.25 eV, 1.95 eV and 3.1 eV, to the $^3T_{2g}(F) \rightarrow {}^3A_{2g}(F)$, $^3T_{1g}(F) \rightarrow {}^3A_{2g}$ and $^3T_{1g}(F) \rightarrow {}^3A_{2g}(F)$ electronic transitions, respectively. Assuming the maximum of the elastic peak as the relative zero energy, it is possible to compare the *d-d* region obtained by both RIXS and UV-Vis spectroscopies (inset in Figure 7). As a result of this comparison, it is worth to note that RIXS completes our knowledge about the *d-d* region, being able to prove the presence and to identify the exact energy location of the third transition at 3.1 eV, which was not clearly observable by means of optical spectroscopy. The whole set of *d-d* transitions expected for a Ni(II) ion in a distorted O_h symmetry has so been disclosed. This result is achievable because the atomic selectivity towards Ni of the RIXS technique does not excite the ligand $\pi \rightarrow \pi^*$ transitions, that overshadow the *d-d* transition at higher energy in Ni(II). Thus, even if its resolution is much worse than that granted by UV-Vis spectroscopy (scattered points in the inset of Figure 7 allow to appreciate the RIXS resolution), due to its element selectivity, RIXS can provide us specific information about the desired element.

3. Experimental Section

3.1. Materials and Methods. The 4,4'-bis(1*H*-pyrazol-4-yl)biphenyl ligand (H_2PBP) and the corresponding coordination compound $[Ni_8(OH)_4(OH_2)_2(PBP)_6]\cdot$nSolv (**NiPBP**) were prepared as reported previously.[15] Prior to any subsequent investigation, the quality and purity of **NiPBP** was checked by means of X-ray powder diffraction.

3.2. Low Pressure Gas Sorption Measurements. Glass sample-tubes of a known weight were loaded with approximately 100 mg of sample, in the form of loose powder, and sealed using a

TranSeal. The sample was degassed at 393 K overnight and, subsequently, at 453 K for 2 h on a Micromeritics ASAP2020 analyzer (Micrometrics Instruments Corp., Norcross, GA) until the outgas rate was less than 2 mTorr/min. The sample tube containing the degassed sample was weighed again and then transferred back to the analyzer. The outgas rate was again confirmed to be less than 2 mTorr/min. N_2 isotherms were measured at 77 K in a liquid nitrogen bath using UHP-grade gas sources. All the reported quantities are affected by an error of 10%, mainly due to the pressure determination.

3.3. High Pressure Gas Sorption Measurements. Excess H_2 adsorption isotherms were collected by volumetric measurements carried out at 77 K, over the 0–80 bar pressure range, on a PCI instrument supplied by Advanced Materials Corporation (Pittsburgh PA) which is capable of collecting isotherms over a wide range of pressures (0.01-200 bar) and temperatures (77-773 K). Ultra pure 6.0 grade H_2 (99.9999%V; Rivoira) was used to the purpose. A modified version of the Benedict-Webb-Rubin equation of state was used to correctly take into account the non ideal behaviour of the H_2 gas in the measurement conditions. In a typical measurement, about 500 mg of **NiPBP**, in the form of loose powder, were activated under ultra high vacuum (residual pressure < 10^{-4} mbar) at 393 K overnight and, subsequently, at 453 K for 2 h. The activated material was then transferred, under protected atmosphere, in the measurement cell. The skeletal sample density was retrieved from the helium isotherm measured on the sample at 293 K in the 0-20 bar range, by means of the intelligent gravimetric analyzer IGA-002, supplied by Hiden Analytical Ltd, UK.

The absolute adsorption, n_{abs}, was calculated using the following relationship:

$$n_{abs} = n_{exc} + V_{pores} \cdot \rho_{gas} \quad (1)$$

where n_{exc} is the excess uptake, V_{pores} is the pore volume of the sample and ρ_{gas} is the density of pure H_2 gas as retrieved through the Benedict-Webb-Rubin equation. V_{pores} is calculated from the experimental skeletal density of the sample, d_{sk}, and the crystallographically determined bulk density of the sample, d_{bulk}, using the following expression:

$$V_{pores} = \frac{d_{sk} - d_{bulk}}{d_{sk} d_{bulk}} \quad (2)$$

The absolute volumetric uptake, n_{vol}, was calculated by:

$$n_{vol} = Q_{ads} \cdot d_{bulk} \quad (3)$$

where Q_{ads} represents the total H_2 adsorbed (in mmol/g).

3.4. Infrared Spectroscopy. IR spectroscopy measurements were carried out by taking advantage of a cryogenic cell obtained by properly modifying a closed-circuit liquid helium Oxford CCC 1204 cryostat, which allows the infrared monitoring of the adsorbed probes under controlled temperature (between 300 and 14 K) and pressure conditions. Thin self-supported wafers of **NiPBP** were prepared in the cryogenic cell and outgassed under high vacuum (residual pressure < 10^{-4} mbar) at 453 K for 2 h. The spectra were recorded on a Bruker Equinox 55 FTIR spectrometer (equipped with an MCT cryogenic detector) mounting a sample compartment modified to accommodate the cryogenic head; 128 interferograms (recorded at 1 cm^{-1} resolution) were typically averaged for each spectrum. A typical IR experiment consisted of three steps: (i) 40 mbar of the gas probe (H_2 or CO) were initially dosed on the sample at 300 K. (ii) A set of IR spectra was then recorded *in situ* while lowering the temperature down to 14 K for H_2 or to 60 K for CO. The samples were then left at the lowest temperature reached for one night, allowing the system to reach the equilibrium conditions. (iii) A set of IR spectra was finally recorded while stepwise outgassing the material.

3.5. UV-Vis Spectroscopy. Diffuse reflectance UV-Visible spectra were recorded on a Cary 5000 Varian spectrophotometer equipped with a reflectance sphere. A thick self-supported wafer of **NiPBP**, inserted in a homemade quartz cell equipped with an optical window, was preliminary measured and then heated and outgassed under high vacuum (residual pressure < 10^{-4} mbar) at 453 K for 2 h, to acquire the spectrum of the activated sample.

3.6. X-ray Absorption and Emission Spectroscopy. X-ray absorption and emission experiments at the Ni K-edge (8345 eV) were performed at the ID26 beamline of the European Synchrotron Radiation Facility (ESRF). The absorption experiment was performed using a Si(311) monochromator to select the incident beam, collecting the XANES spectrum in fluorescence mode with a photodiode. The resonant inelastic X-ray scattering (RIXS) spectra were measured exciting the sample at the K (1s) absorption pre-edge at 8332 eV (in a simplified view due to the $1s \rightarrow 3d$ quadrupole transition), and analyzing the fluorescence photons with the spectrometer available at ID26, based on Rowland geometry, mounting a Si(551) analyzer crystal and an avalanche photodiode. In order to achieve an energy bandwidth of 400 meV at 8 keV ($\Delta E/E = 5\ 10^{-5}$) a crystal bending radius of 2 m was chosen. This resolution was needed to resolve the *d-d* transition at the lowest energy from the elastic peak. Careful radiation damage studies were performed before collection of the RIXS spectrum. The latter was obtained collecting each point of the spectrum in different spots of the sample, keeping the illumination time per spot below the damage limit. Because of the weakness of the investigated features and because of the low photon flux imposed by the desired energy resolution, a total acquisition time of 6 h was needed to obtain sufficient counting statistics. The RIXS spectrum was acquired up to an energy transfer ($E_{ex} - E_{fluo}$) of 15 eV, being E_{ex} and E_{fluo} the excitation energy (defined by the primary monochromator) and the energy of the emitted fluorescence photon (defined by the Rowland spectrometer), respectively.

4. Conclusions

The foregoing results afford a coherent picture of the gas adsorption properties of **NiPBP**, [$Ni_8(\mu_4\text{-}OH)_4(\mu_4\text{-}OH_2)_2(\mu_4\text{-}PBP)_6$], as probed by low and high pressure adsorption measurements of N_2 and H_2, respectively, at 77 K. The results emerging from the N_2 isotherm confirm the accessibility of almost all the void volume, in terms of both octahedral and tetrahedral cavities. Beside recurring to the "average" structural features, the adsorptive performances of **NiPBP** has been interpreted through the local details on the inorganic nodes, provided by combining electronic spectroscopy to X-ray (absorption and emission) spectroscopy, and through the information emerged from variable temperature IR spectroscopy. Thus, the absence of exposed metal sites suggested by the not-so-exciting H_2 uptake could be further corroborated by the response of the material toward CO and H_2, as monitored by IR.

NiPBP thus represents a valuable *proof-of-concept* PCP, which demonstrate that a complete and coherent picture, relating ("average" and local) structural aspects to adsorptive properties, can be successfully retrieved through an optimized combination of complementary solid state techniques.

References

1 See e.g.: (*a*) L. R. MacGillivray, Ed. Metal-Organic Frameworks: Design and Application; John Wiley & Sons Inc: Hoboken, New Jersey, 2010. (*b*) M. Schöder, Ed. Functional Metal-Organic Frameworks: Gas Storage, Separation and Catalysis; Springer: Berlin, New York, 2010. (*c*) T. Scott, S. T. Meek, J. A. Greathouse and M. D. Allendorf, *Adv. Mater.*, 2010, **23**, 249. (*d*) J. R. Long and O. M. Yaghi, *Chem. Soc. Rev.*, 2009, **38**, 1213.

2 O. M. Yaghi and H. L. Li, *J. Am. Chem. Soc.*, 1995, **117**, 10401.

3 (*a*) L. J. Murray, M. Dincă and J. R. Long, *Chem. Soc. Rev.*, 2009, **38**, 1294. (*b*) D. M. D'Alessandro, B. Smith and J. R. Long, *Angew. Chem. Int. Ed.*, 2010, **49**, 6058. (*c*) J. Sculley, D. Yuan and H.-C. Zhou, *Energy Environ. Sci.*, 2011, **4**, 2721. (*d*) Y. H. Hu and L. Zhang, *Adv. Mater.*, 2010, **22**, E117.

4 See e.g. (*a*) D. Liu and C. Zhong, *J. Mater. Chem.*, 2010, **20**, 10308. (*b*) A. U. Czaja, N. Trukhan and U. Muller, *Chem. Soc. Rev.*, 2009, **38**, 1284. (*c*) J. R. Li, R. J. Kuppler and H. C. Zhou, *Chem. Soc. Rev.*, 2009, **38**, 1477.

5 See e.g. (*a*) S. Achmann, G. Hagen, J. Kita, I. M. Malkowsky, C. Kiener and R. Moos, *Sensors*, 2009, **9**, 1574. (*b*) B. Chen, L. Wang, F. Zapata, G. Qian and E. B. Lobkovsky, *J. Am. Chem. Soc.*, 2008, **130**, 6718. (c) W. J. Rieter, K. M. L. Taylor and W. Lin, *J. Am. Chem. Soc.*, 2007, **129**, 9852.

6 See e.g. (*a*) A. Corma, H. García and F. X. Llabres i Xamena, *Chem. Rev.*, 2010, **110**, 4606. (*b*) J. Y. Lee, O. K. Farha, J. Roberts, K. A. Scheidt, S. B. T. Nguyen and J. T. Hupp, *Chem. Soc. Rev.*, 2009, **38**, 1450. (*c*) D. Farrusseng, S. Aguado and C. Pinel, *Angew. Chem. Int. Ed.*, 2009, **48**, 7502. (*d*) L. Q .Ma, C. Abney and W. B. Lin, *Chem. Soc. Rev.*, 2009, **38**, 1248.

7 See e.g. (*a*) F. Ke, Y.–P. Yuan, L.-G. Qiu, Y.–H. Shen, A.–J. Xie, J.–F. Zhu, X.–Y. Tian and L. D. Zhang, *J. Mater. Chem.*, 2011, **21**, 3843. (*b*) P. Horcajada, T. Chalati, C. Serre, B. Gillet, C. Sebrie, T. Baati, J. F. Eubank, D. Heurtaux, P. Clavette, C. Kreuz, J. S. Chang, Y. K. Hwang, V. Marasud, P. N. Bories, L. Cynober, S. Gil, G. Feréy, P. Couvreur and R. Gref, *Nat. Mater.*, 2010, **9**, 172. (*c*) I. Imaz, M. Rubio-Martínez, L. García-Fernández, F. García, D. Ruiz-Molina, J. Hernando, V. Puntes and D. Maspoch, *Chem. Commun*., 2010, **46**, 4737. (*d*) B. Xiao, P. S. Wheatley, X. B. Zhao, A. J. Fletcher, S. Fox, A. G. Rossi, I. L. Megson, S. Bordiga, L. Regli, K. M. Thomas and R. E. Morris, *J. Am. Chem. Soc.*, 2007, **129**, 1203.

8 N. Masciocchi, S. Galli and A. Sironi in Techniques in Inorganic Chermistry; J. P. Fackler, L. Falvello, Eds.; CRC Press Taylor and Francis: Boca Raton, Florida, 2010.

9 S. Bordiga, F. Bonino, K. P. Lillerud and C. Lamberti, *Chem. Soc. Rev.*, 2010, **39**, 4885.

10 (a) U. Bergmann and P. Glatzel, *Photosynth. Res*., 2009, **102**, 255. (b) G. Smolentsev, A. V. Soldatov, J. Messinger, K. Merz, T. Weyhermuller, U. Bergmann, Y. Pushkar, J. Yano, V. K. Yachandra and P. Glatzel, *J. Am. Chem. Soc*., 2009, **131**, 13161. (c) V. A. Safonov, L. N. Vykhodtseva, Y. M. Polukarov, O. V. Safonova, G. Smolentsev, M. Sikora, S. G. Eeckhout and P. Glatzel, *J. Phys. Chem. B*, 2006, **110**, 23192. (d) J. C. Swarbrick, Y. Kvashnin, K. Schulte, K. Seenivasan, C. Lamberti and P. Glatzel, *Inorg. Chem*., 2010, **49**, 8323. (e) N. Lee, T. Petrenko, U. Bergmann, F. Neese and S. DeBeer, *J. Am. Chem. Soc*., 2010, **132**, 9715. (f) S. G. Eeckhout, O. V. Safonova, G. Smolentsev, M. Biasioli, V. A. Safonov, L. N. Vykhodtseva, M. Sikora and P. Glatzel, *J. Anal. At. Spectrom*., 2009, **24**, 215. (g) E. Gallo, C. Lamberti and P. Glatzel, *Phys. Chem. Chem. Phys*., 2011, **13**, DOI: 10.1039/c1cp21556f.

11 See e.g. (*a*) F. Bonino, S. Chavan, J. G. Vitillo, E. Groppo, G. Agostini, C. Lamberti, P. D. C. Dietzel, C. Prestipino and S. Bordiga, *Chem. Mater.*, 2008, **20**, 4957. (*b*) C. Lamberti, A. Zecchina, E. Groppo and S. Bordiga, *Chem. Soc. Rev.*, 2010, **39**, 4951.

12 See e.g. (*a*) K. S. Park, Z. Ni, A. P. Côté, J. Y. Choi, R. Huang, F. J. Uribe-Romo, H. K. Chae, M. O'Keeffe and O. M. Yaghi, *Proc. Natl. Acad. Sci. USA*, 2006, **103**, 10186. (*b*) X.-C. Huang, Y.-Y. Lin, J.-P. Zhang and X.-M. Chen, *Angew. Chem. Int. Ed.*, 2006, **45**, 1557. (*c*) Y.-Q. Tian, Y.-M. Zhao, Z.-X. Chen, G.-N. Zhang, L.-H. Weng and D.-Y. Zhao, *Chem. Eur. J.*, 2007, **13**, 4146. (*d*) A. Demessence, D. M. D'Alessandro, M. L. Foo and J. R. Long, *J. Am. Chem. Soc.*, 2009, **131**, 8784.

13 See e.g. (*a*) J. A. Greathouse and M. D. Allendorf, *J. Am. Chem. Soc.*, 2006, **128**, 10678. (*b*) S. S. Kaye, A. Dailly, O. M. Yaghi and J. R. Long, *J. Am. Chem. Soc.*, 2007, **129**, 14176. (*c*) J. J. Low, A. Benin, P. Jakubczak, J. F. Abrahamian, S. A. Faheem and R. R. Willis, *J. Am. Chem. Soc.*, 2009, **131**, 15834.

14 See e.g. (*a*) J.-P. Zhang and S. Kitagawa, *J. Am. Chem. Soc.*, 2008, **130**, 907. (*b*) H. J. Choi, M. Dincă and J. R. Long, *J. Am. Chem. Soc.*, 2008, **130**, 7848. (*c*) H. J. Choi, M. Dincă, A. Dailly and J. R. Long, *Energy Environ. Sci.*, 2010, **3**, 117. (*d*) S. Galli, N. Masciocchi, V. Colombo, A. Maspero, G. Palmisano, F. J. López-Garzón, M. Domingo-García, I. Fernández-Morales, E. Barea and J. A. R. Navarro, *Chem. Mater*., 2010, **22**, 1664. (*e*) V. Colombo, S. Galli, H. J. Choi, G. D. Han, A, Maspero, G. Palmisano, N. Masciocchi and J. R. Long, *Chem. Sci*., 2011, **2**, 1311.

15 N. Masciocchi, S. Galli, V. Colombo, A. Maspero, G. Palmisano, B. Seyyedi, C. Lamberti and S. Bordiga, *J. Am. Chem. Soc.*, 2010, **132**, 7902.

16 The inner size of the cavity has been estimated as twice the distance between the centre of the cavity and the nearest atom, A, decorating its walls. The proper correction for the vdW radius of A has been applied.

17 Calculated with PLATON (A. L. Spek, *J. Appl. Cryst.*, 2003, **36**, 7) after solvent removal.

18 S. J. Gregg and K. S. W. Sing, Adsorption, Surface Area and Porosity. In Academic Press: London, 1982; p. 113.

29 S. Figueroa-Gerstenmaier, C. Daniel, G. Milano, J. G. Vitillo, O. Zavorotynska, G. Spoto, and G. Guerra, *Macromolecules*, 2010, **43**, 8594.

19 (*a*) A. G. Wong-Foy, A. J. Matzger, O. M. Yaghi, *J. Am. Chem. Soc.* 2006**, 128**, 3494. (*b*) J. R. Long, M. Dinca, *Angew. Chem. Int. Ed.* 2008, **47**, 6766.

20 S. R. Miller, G. M. Pearce, P. A. Wright, F. Bonino, S. Chavan, S. Bordiga, I. Margiolaki, N. Guillou, G. Férey, S. Bourrelly and P. L. Llewellyn, *J. Am. Chem. Soc*., 2008, **130**, 15967.

21 J. G. Vitillo, L. Regli, S. Chavan, G. Ricchiardi, G. Spoto, P. D. C. Dietzel, S. Bordiga and A. Zecchina, *J. Am. Chem.*

Soc., 2008, **130**, 8386.
22 B. N. Figgis and M. A. Hitchman, Ligand Field Theory and Its Applications; Wiley: New York, 2000.
23 B. Fromme, d-d Excitations in Transition Metal Oxides; Springer-Verlag: Berlin, 2001.
24 J. Estephane, E. Groppo, A. Damin, J. G. Vitillo, D. Gianolio, C. Lamberti, S. Bordiga, C. Prestipino, S. Nikitenko, E. A. Quadrelli, M. Taoufik, J. M. Basset, and A. Zecchina, *J. Phys. Chem.* C, 2009, **113**, 7305
25 (*a*) P. Glatzel and U. Bergmann, *Coord. Chem. Rev*., 2005, **249**, 65. (*b*) P. Glatzel, M. Sikora, G. Smolentsev and M. Fernandez-Garcia, *Catal. Today*, 2009, **145**, 294.
26 S. Huotari, T. Pylkkänen, G. Vankó, R. Verbeni, P. Glatzel and G. Monaco, *Phys. Rev. B*, 2008, **78**, Art. N. 041102(R).
27 (*a*) S. Chavan, J. G.Vitillo, E. Groppo, F. Bonino, C. Lamberti, P. D. C. Dietzel and S. Bordiga, *J. Phys. Chem. C*, 2009, **113**, 3292. (*b*) S. Chavan, F. Bonino, J. G. Vitillo, E. Groppo, C. Lamberti, P. D. C. Dietzel, A. Zecchina and S. Bordiga, *Phys. Chem. Chem. Phys.*, 2009, **11**, 9811.
28 A. Shukla, J. P. Rueff, J. Badro, G. Vankó, A. Mattila, F. M. F. de Groot and F. Sette, *Phys. Rev. B*, 2003, **67**, Art. N. 081101(R).